

See discussions, stats, and author profiles for this publication at: <https://www.researchgate.net/publication/244153960>

# Photoelectrochemical oxidation of salicylic acid and salicylaldehyde on titanium dioxide nanotube arrays

ARTICLE *in* ELECTROCHIMICA ACTA · MAY 2009

Impact Factor: 4.5 · DOI: 10.1016/j.electacta.2009.01.077

---

CITATIONS

28

---

READS

52

## 5 AUTHORS, INCLUDING:



Jiali Wen

Lakehead University Thunder Bay Campus

12 PUBLICATIONS 297 CITATIONS

SEE PROFILE



Robert Matthew Asmussen

Pacific Northwest National Laboratory

21 PUBLICATIONS 230 CITATIONS

SEE PROFILE



Aicheng Chen

Lakehead University Thunder Bay Campus

157 PUBLICATIONS 4,839 CITATIONS

SEE PROFILE



# Photoelectrochemical oxidation of salicylic acid and salicylaldehyde on titanium dioxide nanotube arrays

Min Tian, Brian Adams, Jiali Wen, R. Matthew Asmussen, Aicheng Chen<sup>\*,1</sup>

Department of Chemistry, Lakehead University, Thunder Bay, Ontario P7B 5E1, Canada

## ARTICLE INFO

### Article history:

Received 17 December 2008

Received in revised form 27 January 2009

Accepted 28 January 2009

Available online 5 February 2009

### Keywords:

Photoelectrocatalysis

Salicylic acid

TiO<sub>2</sub> nanotubes

UV–vis spectroscopy

Quantum computation

## ABSTRACT

We report on the kinetics of photoelectrochemical oxidation of salicylic acid (SA) and salicylaldehyde (SH) on titanium dioxide nanotube arrays. The TiO<sub>2</sub> nanotubes were prepared by the electrochemical oxidation of titanium substrates in a nonaqueous electrolyte (DMSO/HF). Scanning electron microscopy (SEM) was employed to examine the morphology of the formed nanotubes. Linear voltammetry was used to study the electrochemical and photoelectrochemical behavior of the synthesized TiO<sub>2</sub> nanotube arrays. The photoelectrochemical oxidation of SA and SH on the TiO<sub>2</sub> nanotubes was monitored by *in situ* UV–vis spectroscopy, showing that the kinetics of the photoelectrochemical oxidation of SA and SH follows pseudo first-order and that the rate constant of SH oxidation is 1.5 times larger than that of SA degradation. Quantum chemical calculations based on the DFT method were performed on SA and SH to address the large difference in kinetics. The relatively higher  $E_{\text{LUMO}} - E_{\text{HOMO}}$  makes SA more stable and thus more difficult to be oxidized photoelectrochemically. The impact of temperature and initial concentrations on the kinetics of SA and SH photoelectrochemical degradation was also investigated in the present work.

© 2009 Elsevier Ltd. All rights reserved.

## 1. Introduction

It is known that salicylic acid (SA) has an ototoxic effect and can induce transient hearing loss in zinc-deficient individuals. It can also cause fetal abnormalities and central nervous system depression if swallowed, inhaled or absorbed through skin. Salicylic acid has been identified as a water pollutant which originates from the manufacturing activities of paper milling, cosmetic industries and as a landfill leachate. Thus, there is great interest in studying the kinetics of the degradation of SA in order to develop advance oxidation techniques to effectively treat the SA pollutant for the purification of wastewater and groundwater.

A variety of techniques have been proposed for wastewater treatment including electrochemical oxidation [1,2], activated electrosorption [3], chemical oxidation, and biological digestion [4]. Heterogeneous photocatalysis is a promising alternative technique for eliminating organic pollutants from wastewater [5–8]. Among various oxide semiconductor photocatalysts, titania (TiO<sub>2</sub>) is one of the most promising photocatalysts [9–12] because of its biological and chemical inertness, cost effectiveness, and the strong oxidizing power of its photogenerated holes [13,14]. TiO<sub>2</sub> has three natural phases: brookite, anatase and rutile; anatase is commonly consid-

ered to be the most active phase as a photocatalyst [15,16]. When TiO<sub>2</sub> is irradiated with near UV light ( $\lambda < 400$  nm), the ensemble of the electrons are excited from the valence band to the conduction band, generating electron–hole pairs which initiate the subsequent surface catalytic reactions. The generated electron–hole pairs have the tendency to recombine; this lowers the photocatalytic efficiency. TiO<sub>2</sub> suspension is widely used due to its large surface area/volume ratio which improves the photocatalytic efficiency. However, there is a serious drawback associated with this approach: it is tedious and costly to recycle TiO<sub>2</sub> suspensions from the treated wastewater, making it undesirable for large scale treatment. Using supported semiconductor films is an alternative solution to overcome the recycling problem. However, when photocatalyst films are used, the surface area exposed to the liquid phase is reduced by 2–3 orders of magnitude compared to powders. The diffusion boundary conditions change from binary collisions to that of a particle against a wall; and mass transfer can become a limiting step. It has been shown that using TiO<sub>2</sub> nanostructures with a high surface area can effectively improve the photocatalytic efficiency [17]. In addition, with TiO<sub>2</sub> nanostructures, the recombination between the photogenerated charge carriers can be effectively suppressed by applying an external potential bias [18,19], further increasing the efficiency of wastewater treatments.

In the present study, for the first time, we report on the kinetics of the photoelectrochemical oxidation of SA and its related compound, salicylaldehyde (SH), on Ti-supported TiO<sub>2</sub> nanotube arrays. SA and SH were chosen as model organic pollutants since they can

\* Corresponding author. Tel.: +1 807 3438318; fax: +1 807 3467775.

E-mail address: [aicheng.chen@lakeheadu.ca](mailto:aicheng.chen@lakeheadu.ca) (A. Chen).

<sup>1</sup> ISE member.

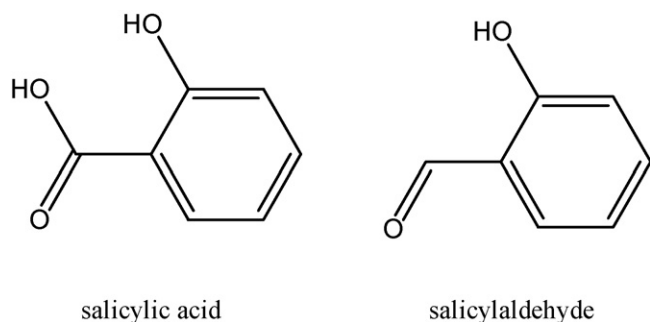


Fig. 1. Chemical structure of salicylic acid and salicylaldehyde.

be considered as typical representatives of the soluble aromatic compounds [20,21]. The molecular structure of SA and SH is shown in Fig. 1. SA has both intramolecular and intermolecular hydrogen bonds, while SH contains only intramolecular hydrogen bonds. UV–vis spectroscopy was employed to *in situ* monitor the time-dependent concentration changes and to determine the kinetics of the photoelectrocatalytic oxidation of SA and SH.

## 2. Experimental

### 2.1. Materials

SA and SH were purchased from Aldrich and used as received. All other chemicals were of reagent grade and were used as supplied. The water (18.2 MΩ cm) used to prepare all solutions was purified by a Nanopure Diamond® water system. Stock solutions were made by dissolving the SA and SH in 0.5 M H<sub>2</sub>SO<sub>4</sub> solution. Subsequent concentrations were obtained by diluting the stock solution with 0.5 M H<sub>2</sub>SO<sub>4</sub> solution.

### 2.2. Preparation and characterization of TiO<sub>2</sub> nanotubes

Pure Ti substrates were degreased by being sonicated in acetone for 10 min and then in the pure water for another 10 min. The Ti substrates were then etched in 18% hydrochloric acid at 85 °C for 15 min. The etched titanium plate was rinsed thoroughly with pure water and then anodized in dimethyl sulfoxide (DMSO) with 2% HF at 40 V for 8 h [5,22]. After electrochemical treatment, the samples were rinsed thoroughly with pure water and dried in an argon stream. In order to achieve a defined anatase structure, the samples were baked at 450 °C for 1 h. The synthesized TiO<sub>2</sub> photocatalysts were characterized by SEM (JEOL JSM 5900LV).

### 2.3. Photoelectrochemical experiments

An EG&G 2273 potentiostat/galvanostat was used to apply an anodic potential bias during the photoelectrochemical degradation of SA and SH. The TiO<sub>2</sub> nanotubes synthesized in this study were used as the working electrode and the counter electrode was a Pt coil. Before each experiment the counter electrode was cleaned by flame annealing and then quenched with pure water. The reference electrode was an Ag/AgCl electrode. The solution in the cell was continuously stirred with a small magnetic stirrer bar. An ADAC Systems™ Cure Spot™ 50 UV spot lamp with three main peaks of emission at around 365, 405 and 435 nm and two small peaks of emission at around 315 and 330 nm was used for the irradiation of the TiO<sub>2</sub> nanotubes. The UV–visible light, with an intensity of ca. 2 mW/cm<sup>2</sup>, was introduced into the cell using fiber optic cable placed above the electrode. The distance between the light source and the electrode surface was 1 cm. *In situ* UV–spectra were recorded by an EPP2000C spectrometer coupled with a dipping

probe connected by fiber optic cables. The experimental temperatures were controlled by a Fisher thermostat.

### 2.4. Kinetics of SA and SH photocatalytic degradation

The kinetics of the photocatalytic oxidation of organics can be analyzed by the Langmuir–Hinshelwood model [23,24]:

$$-\frac{dC}{dt} = k_r \frac{k_a C}{1 + k_a C} \quad (1)$$

where  $-(dC/dt)$  is the photocatalytic oxidation rate,  $k_r$  is the photocatalytic oxidation rate constant,  $k_a$  is the adsorption equilibrium constant, and  $t$  is the reaction time. If the product of  $k_a$  and  $C$  is significantly smaller than 1, the above equation can be simplified to a first-order reaction:

$$-\frac{dC}{dt} = k_r k_a C \quad (2)$$

Consequently an integrated form of Eq. (2) can be represented as follows:

$$\ln \left( \frac{C_0}{C} \right) = k_{app} t \quad (3)$$

where  $k_{app} = k_r k_a$  is the apparent rate constant in min<sup>-1</sup>. The  $k_{app}$  value can be obtained by plotting  $\ln(C/C_0)$  vs.  $t$ .

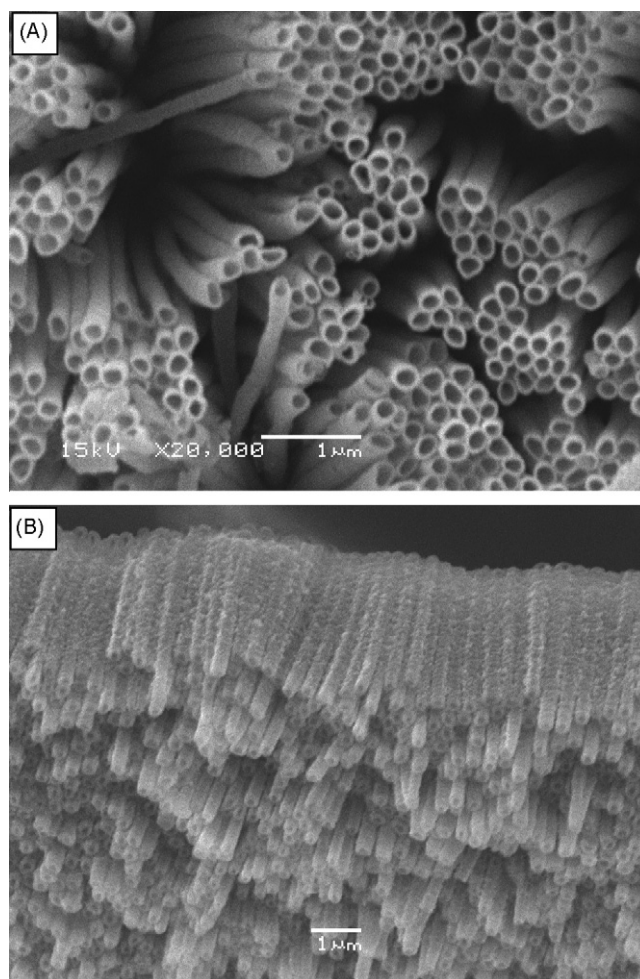


Fig. 2. SEM images of the titanium oxide nanotubes prepared at 40 V for 8 h in DMSO + 2% HF: top view (A) and side view (B).

## 2.5. Quantum chemical calculations

A quantum-mechanical program, Gaussian 03, was used for the molecular modeling. The calculation was based on the B3LYP method [25] and 6-31\*G basis set [26] at ambient temperature. This basis set has provided accurate geometry and electronic properties for a wide range of organic compounds. B3LYP, one of the density functional theory (DFT) methods, defines the exchange function as a linear combination of Hartree-Fock, local, and gradient-corrected exchange terms; this exchange function is then combined with the local and/or the gradient-corrected correlation function of Lee, Yang and Pam (LYP) [27]. All quantum calculations were carried out with full geometry optimizations. The following quantum chemical descriptors were calculated: the energy of the highest occupied molecular orbital ( $E_{\text{HOMO}}$ ), the energy of the lowest unoccupied molecular orbital ( $E_{\text{LUMO}}$ ), and the dipole moment ( $\mu$ ).

## 3. Results and discussion

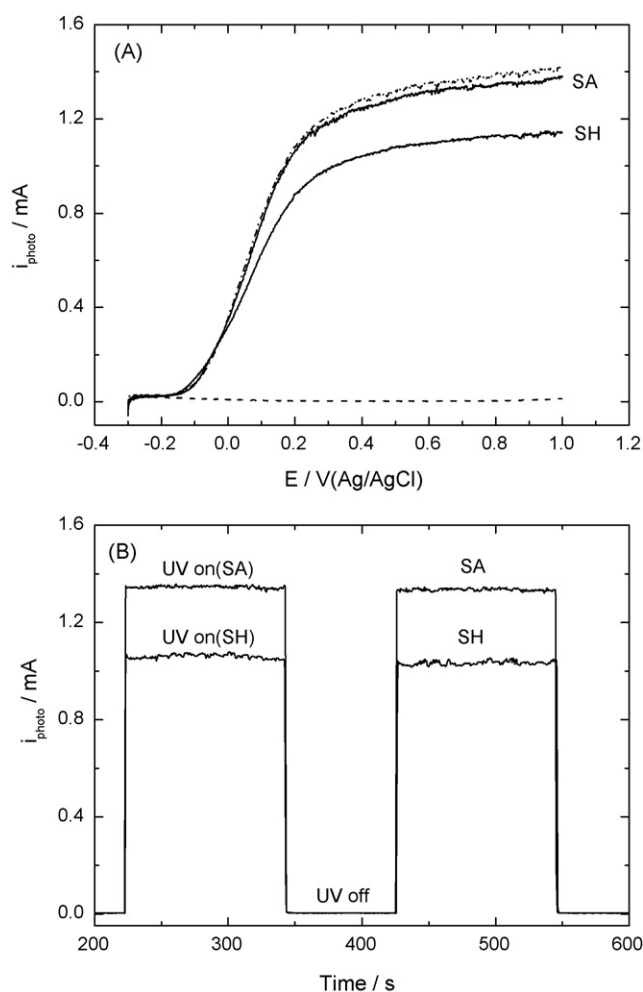
### 3.1. Surface characterization of the TiO<sub>2</sub> nanotubes

Fig. 2 shows typical SEM images of the top (A) and side view (B) of the TiO<sub>2</sub> nanotube arrays synthesized by the electrochemical oxidation of the titanium substrates at 40 V for 8 h in a nonaque-

ous electrolyte (DMSO containing 2% HF). From these images, it is evident that the self-organized regular TiO<sub>2</sub> consists of pore arrays with uniform pore diameters of ca. 60 nm and lengths of ca. 6  $\mu\text{m}$ . The long TiO<sub>2</sub> nanotubes grown in this organic solvent can be attributed to the presence of less water which decreases the solubility of TiO<sub>2</sub>. As anatase is known to be the most efficient TiO<sub>2</sub> structure for photocatalysis, the synthesized TiO<sub>2</sub> nanotubes were annealed at 450 °C for 1 h to form the anatase structure.

### 3.2. Electrochemical and photoelectrochemical properties of the TiO<sub>2</sub> nanotubes

Linear voltammetry was employed to study the electrochemical and photoelectrochemical behavior of the synthesized TiO<sub>2</sub> nanotube arrays. Fig. 3A shows the linear voltammograms of the TiO<sub>2</sub> nanotube arrays recorded in a 0.5 M H<sub>2</sub>SO<sub>4</sub> solution without UV irradiation (dashed line) and under the UV irradiation (dotted line); and in 0.5 M H<sub>2</sub>SO<sub>4</sub> solutions in the presence of 30 ppm of SA or SH under the UV irradiation (solid lines). The electrode potential was swept from  $-0.3$  to  $1.0$  V vs. Ag/AgCl at a scan rate of 5 mV/s. TiO<sub>2</sub> is a semiconductor with low electrocatalytic activity. As expected, no measurable current was observed in the investigated potential range without UV irradiation. In contrast, under the UV illumination an anodic current arises when the potential is higher than  $-0.17$  V.



**Fig. 3.** (A) Linear voltammograms of TiO<sub>2</sub> nanotube arrays: in 0.5 M H<sub>2</sub>SO<sub>4</sub> with (dotted line) and without (dashed line) the UV illumination in 0.5 M H<sub>2</sub>SO<sub>4</sub> electrolytes containing 30 ppm of SA or SH (solid lines). Scan rate: 5 mV/s. (B) The transient photocurrent-time profiles of the TiO<sub>2</sub> nanotubes following UV illumination at an applied potential bias of 0.6 V vs. Ag/AgCl.

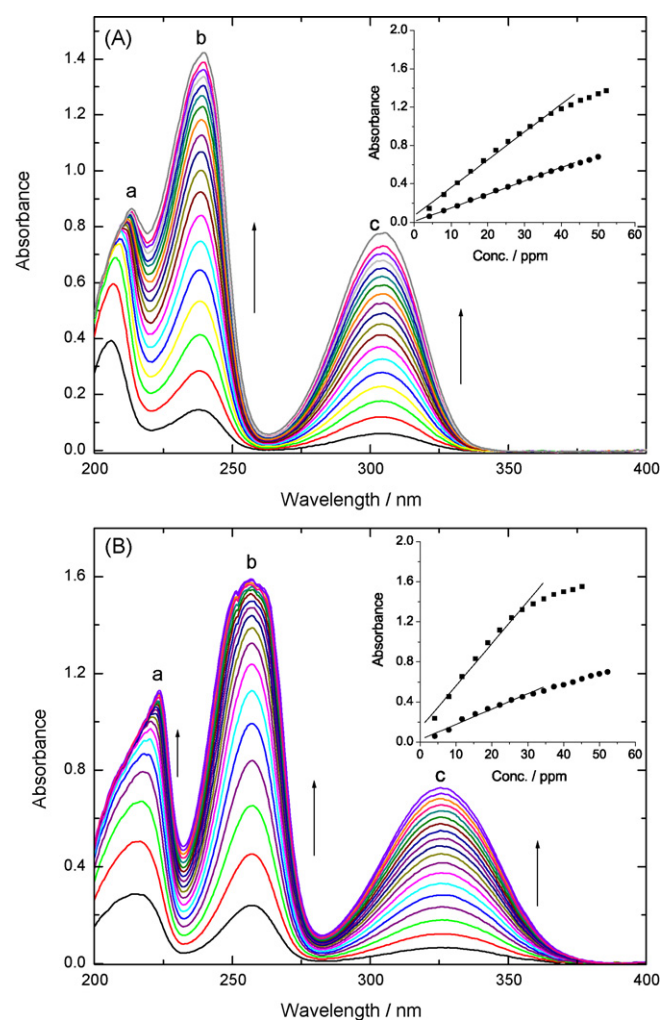


**Fig. 4.** Calibration curves for SA (A) and SH (B). Arrows show the direction of movement of curves. All the spectra are referenced by their corresponding blank 0.5 M H<sub>2</sub>SO<sub>4</sub> aqueous solution. Insets: relationship between absorbance and concentration.



The photocurrent increases significantly with the increase of the potential from  $-0.15$  to  $0.3$  V; and then slightly increases when the electrode potential is further increased. The relationship between the applied potential and the measured photocurrent is consistent with the prediction made by the classical semiconductor theory [28]. The photocurrent originates from the water splitting reaction. Gas evolution was observed on both the  $\text{TiO}_2$  working electrode and the Pt counter electrode. It is interesting to note that the photocurrent only slightly decreases with the addition of SA and that it decreases by  $\sim 20\%$  with the addition of SH. This significant decrease may be due to the fact that UV absorption by SH reduces the photon flux available at the electrode surface, similar to that observed in the photocatalytic oxidation of nitrophenol [5]. As seen in Fig. 3A, the photocurrents reach the maximum at  $0.6$  V, indicating that the applied potential  $0.6$  V can effectively suppress the recombination of the photogenerated electron–hole pairs. The potential bias of  $0.6$  V was thus chosen for all subsequent experiments. We further studied the photocurrent transients at the applied electrode potential of  $0.6$  V vs. Ag/AgCl by switching the UV light on and off. The duration of light pulses was set at  $120$  s, followed by dark current measurements for  $80$  s. As shown in Fig. 3B, the response of the photocurrent to the UV irradiation is very quick and that the photocurrent in the presence of SH ( $1.07$  mA) is lower than that in the presence of SA ( $1.36$  mA). This is consistent with the observation in the linear voltammetric study shown in Fig. 3A. The achieved high photocurrents compared to the relatively low intensity

( $\sim 2$  mW/cm<sup>2</sup>) of the illuminated UV light reveals that the synthesized  $\text{TiO}_2$  nanotube arrays possess high photocatalytic activities.

### 3.3. Calibration for SA and SH

A univariate calibration was conducted in order to convert the UV absorbance into concentration. Fig. 4 shows the concentration-dependence of the spectral absorbance of SA (A) and SH (B) recorded in the range of  $200$ – $600$  nm. Three bands centered at  $215$  nm (Peak a),  $238$  nm (Peak b) and  $304$  nm (Peak c) are observed in Fig. 4A. The inset of Fig. 4A presents the plots of the intensity of Peak b and Peak c vs. the concentration of SA, showing that the linear dynamic range for SA is  $0$ – $50$  ppm with the linear regression equations  $A_b = 0.029c$  (ppm) +  $0.060$  with a correlation coefficient of  $0.996$ ; and  $A_c = 0.014c$  (ppm) +  $0.009$  with a correlation coefficient of  $0.999$ . As seen in Fig. 4B, three strong bands centered at  $220$  nm (Peak a),  $257$  nm (Peak b) and  $327$  nm (Peak c) appear in the SH spectra over a wavelength range from  $200$  nm to  $600$  nm. The absorption of Peaks b and c linearly increases with the increase of the SH concentration. However, there is no linear relationship between Peak a and the concentration of SH and SA. As shown in the inset to Fig. 4B, for Peak b and Peak c, the linear dynamic range is  $0$ – $40$  ppm with the linear regression equations  $A_b = 0.042c$  (ppm) +  $0.136$  (Peak b) and  $A_c = 0.015c$  (ppm) +  $0.021$  (Peak c), both with correlation coefficients of  $0.992$ .

### 3.4. Photoelectrochemical oxidation of SA and SH at $\text{TiO}_2$ nanotubes

Photoelectrochemical oxidation of SA and SH on the  $\text{TiO}_2$  nanotube arrays was monitored by *in situ* UV–vis spectroscopy. Fig. 5A shows the time-dependence of the spectral absorbances taken at

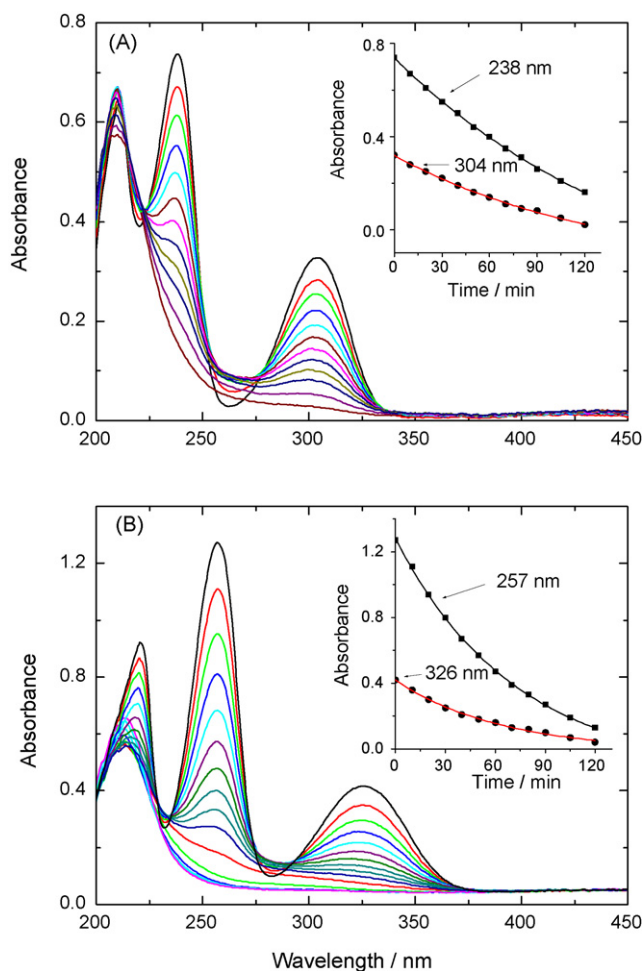


**Fig. 5.** *In situ* scanning-kinetics data for the photoelectrochemical oxidation of 30 ppm SA (A) and SH (B) at the  $\text{TiO}_2$  nanotube arrays in  $0.5$  M  $\text{H}_2\text{SO}_4$ . The applied potential bias was  $0.6$  V (Ag/AgCl). The insets in (A) and (B) show variations of absorbance during the photoelectrochemical oxidation of SA and SH, respectively.

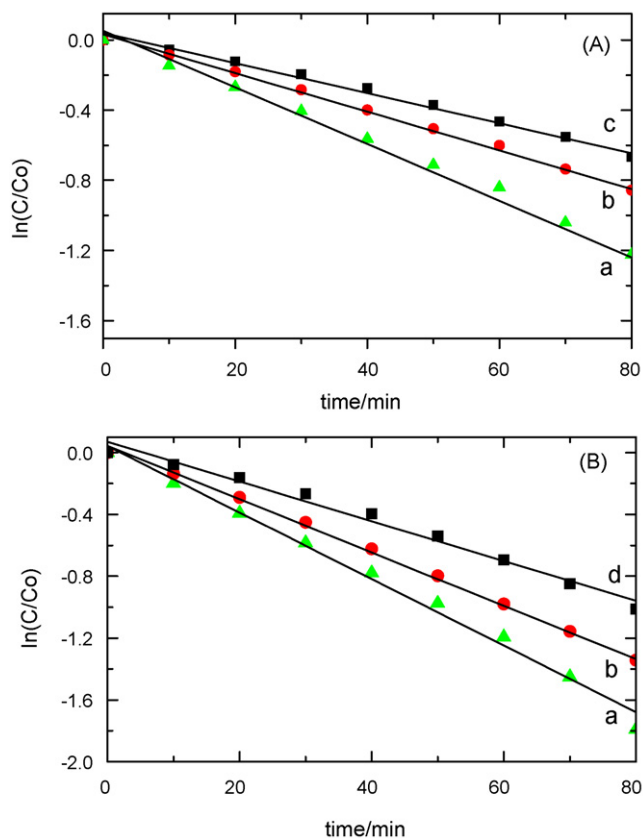


**Fig. 6.** Kinetic plots for photoelectrochemical oxidation of SA (A) and SH (B) at different initial concentrations: (a) 20 ppm; (b) 30 ppm; (c) 50 ppm (SA); (d) 40 ppm (SH).

10 min intervals in the course of the photoelectrochemical oxidation of 30 ppm SA in 0.5 M  $\text{H}_2\text{SO}_4$ . The absorbance of SA at 237 (Peak *b*) and 304 nm (Peak *c*) decreases with the increase of the irradiation time. For instance, the absorbance of Peak *b* approaches 0.14 after 2 h of the photoelectrochemical degradation, corresponding to 83% (i.e.,  $7.2 \times 10^{18}$  molecules) degradation of SA from the solution. As seen in the insert of Fig. 5A, the simulation based on first-order kinetics (solid lines) fits the experimental data very well, showing that the photoelectrochemical oxidation of SA follows first-order kinetics.

Fig. 5B presents the spectral absorbance taken at 10 min intervals during the photoelectrocatalytic oxidation of 30 ppm SH in 0.5 M  $\text{H}_2\text{SO}_4$ . Peak *b* and Peak *c* decrease with time and approach zero after ca. 2 h, indicating almost complete removal of SH (i.e.,  $9.8 \times 10^{18}$  molecules), where Peak *a* centered at ca. 220 nm has a blue shift; its relative absorbance also decreases with the irradiation time. The scanning-kinetics plots obtained at 257 and 326 nm as a function of time for the photoelectrocatalytic oxidation of SH are shown in the inset to Fig. 5B. The simulation, based on first-order kinetics (solid lines) fits the experimental data effectively, showing that the photoelectrochemical oxidation of SH also follows first-order kinetics.

### 3.5. Effect of initial concentration effect

The effect of the initial concentrations of SA and SH on the photoelectrochemical degradation rate was also investigated. Fig. 6

presents the plots of  $\ln(C/C_0)$  of SA (A) and SH (B) vs. the irradiation time for different initial concentrations. The linear relationship of all the plots further confirms that the photoelectrochemical oxidation of SA and SH follows first-order kinetics. The rate constants of the photoelectrochemical oxidation of SA and SH strongly depend on the initial concentrations. For SA, the  $k_{\text{app}}$  decreases from 0.015 to 0.008  $\text{min}^{-1}$  when its initial concentration was increased from 20 to 50 ppm; while the  $k_{\text{app}}$  for the photoelectrochemical oxidation of SH decreases from 0.215 to 0.013  $\text{min}^{-1}$  when the initial concentration of SH was increased from 20 to 40 ppm. Increasing the initial concentration of SA and SH results in a decrease of the rate constant. This might be attributed to: (i) the competition adsorption for active sites from intermediate compounds deriving from the oxidation with the substrate [29]; and (ii) the increase of the UV attenuation with the increase of SA and SH molecules [30]. In addition, at the same initial concentration, the rate constant of the photoelectrochemical oxidation of SH is larger than that of the photoelectrochemical oxidation of SA. For instance, at 30 ppm, the  $k_{\text{app}}$  for SH is 0.017  $\text{min}^{-1}$ , which is 1.5 times larger than that for the photoelectrocatalytic oxidation of SA. This difference can be attributed to: (i) the difference in adsorption behavior between SA and SH; SA can form a six member ring with the  $\text{TiO}_2$  electrode surface, and (ii) the different hydrogen bonds. SA has both intermolecular and intramolecular hydrogen bonds [31]; while only intramolecular hydrogen bonding exists with SH. The overall hydrogen bonding energy of SA is 48.6  $\text{kJ mol}^{-1}$ , which is much higher than that of SH (32.9  $\text{kJ mol}^{-1}$ ) [32,33]. Consequently

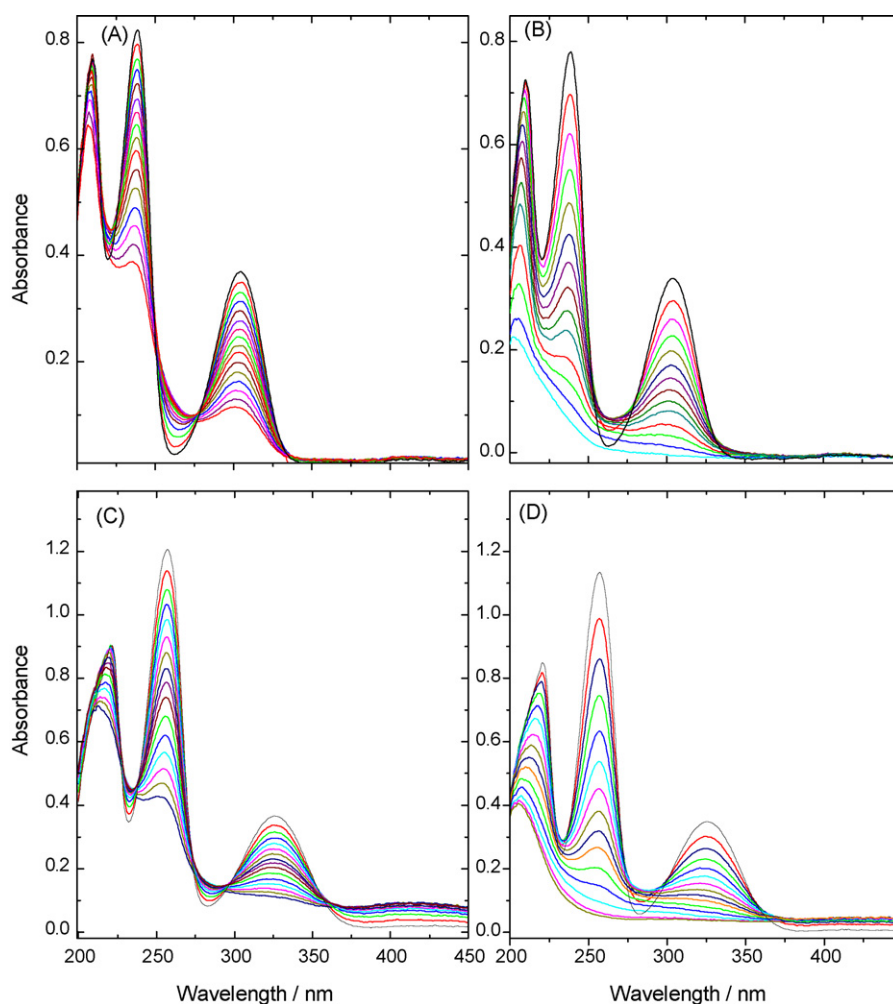


Fig. 7. Scanning-kinetics data for the photoelectrochemical oxidation of SA (A and B) and SH (C and D) at 2 °C (A and C) and 40 °C (B and D).

the photoelectrochemical degradation of SH is much faster than that of SA.

### 3.6. Effect of temperature

We further studied the influence of temperature on the kinetics of the photoelectrochemical oxidation of SA and SH. Fig. 7 presents the spectral absorbance during the photoelectrochemical oxidation of 30 ppm SA (A and B) and SH (C and D) where (A) and (C) are at 2 °C and (B) and (D) are at 40 °C, showing that the photoelectrochemical oxidation of SA and SH is much quicker at the high temperature than at the low temperature. In addition, at the low temperature (2 °C), one isosbestic point at 276 nm is observed in Fig. 7A; and three isosbestic points at 238, 296 and 359 nm are seen in Fig. 7C; while no isosbestic point is observed at the high temperature (Fig. 7B and D). The appearance of the isosbestic points indicates the generation and accumulation of intermediates during the photoelectrochemical oxidation of SA and SH at the low temperature. The changes of the  $C/C_0$  of SA vs. the irradiation time at different temperatures are shown in Fig. 8A; Fig. 8B presents the time-dependent  $C/C_0$  of SH at different temperatures. The linear relationships of the  $\ln(C/C_0)$  vs. the reaction time observed in the inserts of Fig. 8A and B reveal that the photoelectrochemical oxidation of SA and SH at different temperatures follows first-order kinetics. For both SA and SH, the rate constants of the photoelectrochemical oxidation of SA and SH increase with the increase of the applied temperature. Increasing the temperature not only increases

**Table 1**

Molecular properties of SA and SH calculated using B3LYB/6-31G.

	Molecule	
	SA	SH
$E_{\text{HOMO}}$ (eV)	−7.08	−6.97
$E_{\text{LUMO}}$ (eV)	−1.61	−1.96
$\Delta E$ (eV)	5.47	5.01
$E$ (total energy, kcal mol <sup>−1</sup> )	−310893.55	−263955.81
Dipole moment (D)	0.33	5.29
Rate constant (min <sup>−1</sup> )	0.011	0.017

the diffusion of SA and SH molecules from the bulk electrolyte to the electrode surface, but also helps to break the hydrogen bonding. The Arrhenius plots based on the kinetics data determined at 2, 20 and 40 °C yield two straight lines, from which the overall apparent activation energy was estimated, 25.6 and 25.0 kJ mol<sup>−1</sup> for the photoelectrochemical oxidation of SA and SH, respectively. These values are quite close to those for hydroxyl radical reactions, suggesting that the photoelectrochemical oxidation of SA and SH might be governed by the hydroxyl radical reaction [34,35].

### 3.7. Quantum chemical study of SA and SH

Quantum chemical calculation was performed in order to correlate the order of photoelectrochemical reactivity of SA and SH with their electron structure. This has been successfully applied to study the reaction mechanism to solve chemical reaction ambiguities, and to correlate chemical reactivity with molecular orbital (MO) energy [36]. Table 1 presents the results of  $E_{\text{HOMO}}$  (eV),  $E_{\text{LUMO}}$  (eV),  $E_{\text{L}} - E_{\text{H}}$  (eV),  $\mu$  (Debye) and total relative energy (kcal mol<sup>−1</sup>) calculated by the B3LYP method for SA and SH. For comparison, the measured rate constants of the photoelectrochemical oxidation of SA and SH are also listed in the table. It is known that  $E_{\text{HOMO}}$  is often associated with the electron donating ability of the molecule. High values of  $E_{\text{HOMO}}$  indicate a tendency of the molecule to donate electrons to act with acceptor molecules with low energy empty molecular orbital.  $E_{\text{LUMO}}$  represents the ability of a molecule to accept electrons. The lower values of  $E_{\text{LUMO}}$  suggest the molecule accepts electrons more easily; while the highest occupied molecular orbital – lowest unoccupied molecular orbital energy  $\Delta E$  (energy gap) serves as a simple measure of chemical stability [37,38]. It is obvious that the substitution of H in the SH by OH results in an increase in the total relative energy (46937 kcal mol<sup>−1</sup>) and the energy difference  $\Delta E$  (0.5 eV). The higher total relative energy and energy gap ( $\Delta E$ ) of SA make it more stable [38,39] and thus more difficult to degrade. This is consistent with the kinetic results of the photoelectrochemical oxidation of SA and SH.

## 4. Conclusions

In summary, the TiO<sub>2</sub> nanotube arrays grown by electrochemical oxidation of Ti substrates in a DMSO/HF solution show high photoelectrocatalytic activity towards the degradation of SA and SH. The processes were quantitatively monitored by *in situ* UV–vis spectroscopy. With a 30 ppm SA solution, 83% of SA was photoelectrochemically oxidized over a 2-h period; while, with the same initial concentration, SH was almost completely eliminated over a 2-h period, showing that photoelectrochemical oxidation is a very promising approach for the treatment of SH and SA pollutants. The present study shows that the photoelectrochemical oxidation of SA and SH follows first-order kinetics and that the photoelectrochemical oxidation rate constant strongly depends on the structure of the targeted molecules, initial concentration and the applied temperature. The rate constant of the photoelectrochemical oxidation of SA and SH decreases with the increase of initial concentrations, but

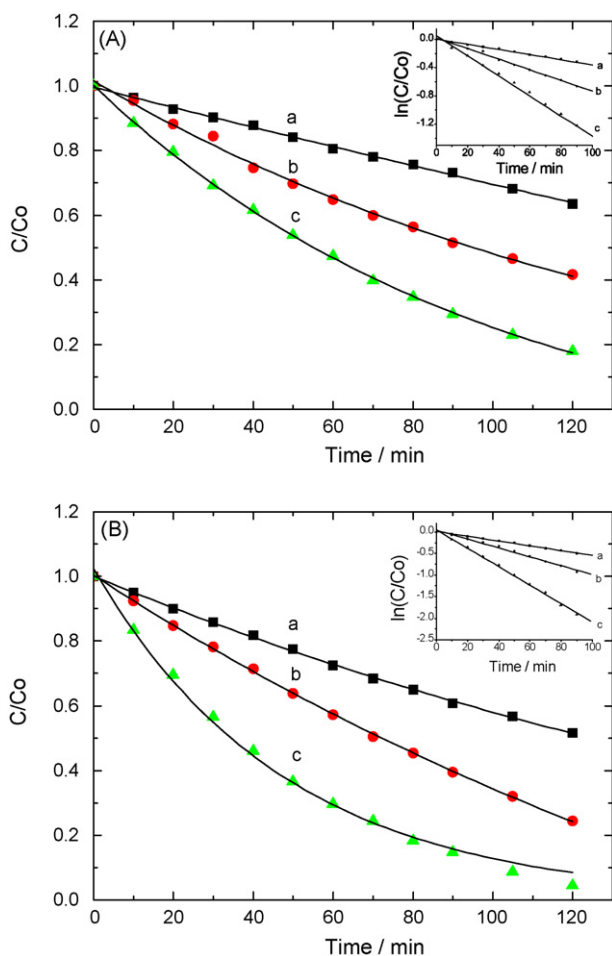


**Fig. 8.**  $C/C_0$  vs. time curves for the photoelectrochemical oxidation of SA (A) and SH (B) at 2 °C (a), 20 °C (b) and 40 °C (c). The insets show the corresponding  $\ln(C/C_0)$ – $t$  curves.

increases with the increase of the applied temperature. The photoelectrochemical oxidation of SH is about 1.5 times quicker than that of SA under the same experimental conditions. This is consistent with the quantum chemical calculations. The higher energy difference  $\Delta E$  of SA makes it more stable and thus more difficult to degrade. Further studies are in progress to elucidate the mechanisms of the photoelectrochemical oxidation of SA and SH.

## Acknowledgements

This work was supported by a Discovery Grant from the Natural Sciences and Engineering Research Council of Canada (NSERC). A. Chen acknowledges NSERC and the Canada Foundation of Innovation (CFI) for the Canada Research Chair Award in Material and Environmental Chemistry.

## References

- [1] M.A. Quiroz, S. Reyna, C.A. Martinez-Huitle, S. Ferro, A. De Battisti, *Appl. Catal.*, B 59 (2005) 259.
- [2] M. Tian, L. Bakovic, A. Chen, *Electrochim. Acta* 52 (2007) 6517.
- [3] E. Ayranci, B.E. Conway, *J. Electroanal. Chem.* 513 (2001) 100.
- [4] O.A. O'Connor, L.Y. Young, *Environ. Toxicol. Chem.* 8 (1989) 853.
- [5] M. Tian, G.S. Wu, B. Adams, J.L. Wen, A.C. Chen, *J. Phys. Chem. C* 112 (2008) 825.
- [6] C.Z. Li, W.B. Choi, C.H. Chuang, *Electrochim. Acta* 54 (2007) 821.
- [7] T.A. Egerton, P.A. Christensen, R.W. Harrison, J.W. Wang, *J. Appl. Electrochem.* 35 (2005) 799.
- [8] C.R. Xiong, K. Balkus Jr., *J. Phys. Chem. C* 111 (2007) 10359.
- [9] G. Wu, J. Wang, D.F. Thomas, A. Chen, *Langmuir* 24 (2008) 3503.
- [10] G. Wu, A. Chen, *J. Photochem. Photobiol. A: Chem.* 195 (2008) 47.
- [11] R. Beranek, J.M. Macak, M. Gartner, K. Meyer, P. Schmuki, *Electrochim. Acta* (2008), doi:10.1016/j.electacta.
- [12] A.G. Muñoz, *Electrochim. Acta* 52 (2007) 4167.
- [13] Y.H. Zhang, H.L. Xu, Y.X. Xu, H.X. Zhang, Y.G. Wang, *J. Photochem. Photobiol. A: Chem.* 170 (2005) 279.
- [14] Y.Y. Hou, J.M. Hu, L. Liu, J.Q. Zhang, C.N. Cao, *Electrochim. Acta* 51 (2006) 6258.
- [15] R.J. Berry, M.R. Muller, *Microchem. J.* 50 (1994) 28.
- [16] J.Q. Li, L.P. Li, L. Zheng, Y.Z. Xian, L.T. Jin, *Electrochim. Acta* 51 (2006) 4942.
- [17] T. Shibata, N. Sakai, K. Fukuda, Y. Ebina, T. Sasaki, *Phys. Chem. Chem. Phys.* 19 (2007) 2413.
- [18] A. Fujishima, K. Honda, *Nature* 238 (1972) 37.
- [19] M. Zlamal, J.M. Macak, P. Schmuki, J. Krysa, *Electrochem. Commun.* 9 (2007) 2822.
- [20] M.E. Calvo, R.J. Candal, S.A. Bilmes, *Catal. Today* 76 (2002) 133.
- [21] S. Tunesi, M.A. Anderson, *J. Phys. Chem.* 95 (1991) 3399.
- [22] S. Yoriya, M. Paulose, O.K. Varghese, G.K. Mor, C.A. Grimes, *J. Phys. Chem. C* 111 (2007) 13770.
- [23] C.S. Turchi, D.F. Ollis, *J. Catal.* 122 (1990) 178.
- [24] M.R. Hoffmann, S.T. Martin, W. Choi, D.W. Bahnemann, *Chem. Rev.* 208 (1995) 69.
- [25] S.G. Zhang, W. Lei, M.Z. Xia, F.Y. Wang, *J. Mol. Struct.* 732 (2005) 175.
- [26] M. Lashgari, M.R. Arshadi, Gh.A. Parsafar, *Corrosion* 61 (2005) 778.
- [27] C. Lee, W. Yang, R.G. Pam, *Phys. Rev. B* 37 (1988) 78.
- [28] A. Hamnett, in: R.G. Compton (Ed.), *Comprehensive Chemical Kinetics*, vol. 27, Elsevier, Amsterdam, 1987, p. 61.
- [29] A. Di Paola, V. Augugliaro, L. Palmisano, G. Pantaleo, E. Savinov, *J. Photochem. Photobiol. A: Chem.* 155 (2003) 207.
- [30] V. Augugliaro, L. Palmisano, M. Schiavello, A. Scillfani, L. Marchese, G. Martra, F. Miano, *Appl. Catal.* 69 (1991) 323.
- [31] M.J. Wójcik, *J. Mol. Struct.* 735 (2005) 225.
- [32] A.K. Tiwari, N. Sathyamurthy, *J. Phys. Chem. A* 110 (2006) 5960.
- [33] F.T.T. Huque, J.A. Platts, *Org. Biomol. Chem.* 1 (2003) 1419.
- [34] R.W. Matthews, *J. Phys. Chem.* 91 (1987) 3328.
- [35] D.W. Chen, A.K. Ray, *Water Res.* 32 (1998) 3223.
- [36] S.M. Bachrach, *Computational Organic Chemistry*, John Wiley & Sons, 2007.
- [37] B.A. Hess, L.J. Schaad, *J. Am. Chem. Soc.* 93 (1971) 2413.
- [38] R.G. Pearson, *J. Am. Chem. Soc.* 110 (1988) 2092.
- [39] N.G. Szwacki, A. Sadrzadeh, B.I. Yakobson, *Phys. Rev. Lett.* 98 (2007) 166804.